Thermochimica Acta 559 (2013) 32–39

Contents lists available at SciVerse ScienceDirect

Thermochimica Acta

journal homepage: www.elsevier.com/locate/tca

Cold-cap reactions in vitrification of nuclear waste glass: Experiments and modeling

Jaehun Chun[a], David A. Pierce[a], Richard Pokorný[b], Pavel Hrma[a,c,*]

[a] Pacific Northwest National Laboratory, Richland, WA 99352, USA
[b] Department of Chemical Engineering, Institute of Chemical Technology in Prague, Technická 5, 166 28 Prague 6, Czech Republic
[c] Division of Advanced Nuclear Engineering, Pohang University of Science and Technology, Pohang, Republic of Korea

ARTICLE INFO

Article history:
Received 5 October 2012
Received in revised form 19 February 2013
Accepted 20 February 2013
Available online 5 March 2013

Keywords:
Cold-cap reactions
Kinetic model
Kissinger method
Nuclear waste glass melting
Heat capacity
Simultaneous differential scanning calorimetry–thermogravimetry

ABSTRACT

Cold-cap reactions are multiple overlapping reactions that occur in the waste-glass melter during the vitrification process when the melter feed is being converted to molten glass. In this study, we used simultaneous differential scanning calorimetry–thermogravimetry (DSC–TGA) to investigate cold-cap reactions in a high-alumina high-level waste melter feed. To separate the reaction heat from both the heat associated with the heat capacity of the feed and experimental artifacts, we employed the run/rerun method, which enabled us to define the degree of conversion based on the reaction heat and to estimate the heat capacity of the reacting feed. Assuming that the reactions are nearly independent and can be approximated by an *n*th order kinetic model, we obtained the kinetic parameters using the Kissinger method combined with least squares analysis. The resulting mathematical simulation of the cold-cap reactions provides a key element for the development of an advanced cold-cap model.

1. Introduction

The cold-cap, or batch blanket, indicates a layer of melter feed, or glass batch, floating on a pool of molten glass in an electrical glass-melting furnace (a melter). For melters processing nuclear waste glass [1–3], unlike furnaces producing commercial glasses, the melter feed is typically slurry containing about 40–60 mass% water. The cold-cap covers 90–95% of the melt surface. The slurry feed is charged on the top of the cold-cap through one or more nozzles. Inside the cold-cap, the dry feed is converted to glass as it moves down through the cold-cap toward its interface with the glass melt underneath (~1000–1100 °C).

The waste itself contains 40–60 elements forming water-soluble salts, amorphous gels, and crystalline minerals. After the waste is mixed with glass-forming and glass-modifying additives, many chemical reactions and phase transitions occur as the mixture components react first in the aqueous slurry and then on subsequent heating during the passage of the feed through the cold cap. The number of intermediate products of cold-cap reactions is large; some of them are not even listed in standard databases. Therefore, identifying individual reactions and investigating their mechanisms appears intractable. Far from resolving molecular mechanisms of individual cold-cap reactions, our simple, yet challenging, task is to develop a "phenomenological" or "apparent" kinetic model as a reasonable approximation for the overall rate of feed-to-glass conversion [3]. Such an "apparent" kinetic model is a necessary ingredient for mathematical modeling of the cold-cap process [1].

Many cold-cap reactions evolve gases. These reactions include the release of chemically bonded water, reactions of nitrates with organics, and reactions of molten salts with solid silica [4–16]. As the gases evolve, the mass of the condensed phases is changing. This change impacts the mass transport equation in the cold cap model, in which it is represented as the mass-based degree of conversion. Pokorný et al. [3] modeled the kinetics of the gas-evolving cold-cap reactions using data from the non-isothermal thermogravimetric analysis (TGA). Their study demonstrated that the cold-cap reactions can be reasonably treated as multiple overlapping reactions that are mutually independent and kinetically simple, neglecting both the dependence between consecutive reactions and the complex responses of some reactants, such as reactions of multicomponent molten salt. They presented the overall reaction rate as a sum of *n*th-order reaction kinetics with the Arrhenius rate coefficients. This model treats the gas-evolving reactions as "apparent" ones, leaving the actual mechanisms unidentified.

For modeling of energy transport within the cold-cap [2], the conversion degree is defined via the reaction heat, measured by the

* Corresponding author at: Pacific Northwest National Laboratory, Richland, WA 99352, USA. Tel.: +1 509 372 4581; fax: +1 509 372 5997.
E-mail addresses: pavelhrma@postech.ac.kr, pavel.hrma@pnnl.gov (P. Hrma).

0040-6031/$ – see front matter © 2013 Elsevier B.V. All rights reserved.
http://dx.doi.org/10.1016/j.tca.2013.02.016

differential scanning calorimetry (DSC), or simultaneous DSC-TGA, normalized with respect to the total heat of conversion. Similar to the analysis of Pokorný et al. [3], we assumed that the cold-cap reactions are independent, kinetically simple, and identifiable as peaks and shoulders in the DSC curve. Apart from the heat of reactions, the response of DSC, or simultaneous DSC-TGA, includes a baseline deviation caused by equipment asymmetries. The sources of these asymmetries are the heat capacity of the sample that is not compensated for by the inert reference [17] and the temperature distribution in the furnace with respect to the position of the sample carrier. To define the degree of conversion based on the reaction heat, the heat flow related to the heat capacity of the sample must be reasonably subtracted from the overall heat flow [18]. By employing the method used by Primig and Leitner [19], we simultaneously corrected the baseline deviation and obtained heat flows associated with reactions. For simplicity, we call this method the run/rerun method hereafter. The separation of the heat flow solely associated with chemical reactions by the run/rerun method is not perfect because the sample during the rerun is not exactly the same as that in the first run. Fortunately, the heat capacity difference does not appear to be significant (see Section 5.3 for details).

Running the simultaneous DSC-TGA at four different heating rates allowed us to employ Kissinger's method [20] to estimate activation energies of individual reactions and then proceed with estimating the remaining parameters by the least squares method. The kinetic parameters are intended for modeling of the cold-cap process.

2. Background for modeling

Although details in cold-cap reactions are rather complicated, we represent individual reactions with an nth-order kinetic model along with the Arrhenius rate coefficient [3]:

$$\frac{d\alpha_i}{dt} = A_i(1-\alpha_i)^{n_i} \exp\left(-\frac{E_i}{RT}\right) \quad (1)$$

where α_i is the ith reaction conversion degree, A_i is the ith reaction pre-exponential factor, E_i is the ith reaction activation energy, n_i is the ith reaction apparent order, T is the temperature, and R is the gas constant. Assuming that the reactions are mutually independent, we represent the overall reaction rate as a weighted sum of the rates of individual reactions:

$$\frac{d\alpha}{dt} = \sum_{i=1}^{N} w_i \frac{d\alpha_i}{dt} = \sum_{i=1}^{N} w_i A_i (1-\alpha_i)^{n_i} \exp\left(-\frac{E_i}{RT}\right) \quad (2)$$

where α is the overall degree of conversion, N is the number of reactions, and w_i denotes the ith reaction fraction such that $\sum_{i=1}^{N} w_i = 1$.

According to Kissinger [20], E_i can be estimated by determining the temperature of the ith peak maximum, T_{im}, for experiments carried out at different heating rates, $\beta \equiv dT/dt$, using the formula

$$\frac{E_i}{R} = -\frac{d(\ln(\beta/T_{\mathrm{im}}^2))}{d(1/T_{\mathrm{im}})} \quad (3)$$

Pokorný et al. [3] showed that this formula can be applied to gas-evolving cold-cap reactions. When β is constant and $n_i \neq 1$, α_i can be obtained by integrating Eq. (1):

$$\alpha_i = 1 - \left[1 + \frac{(n_i-1)A_i}{\beta}\int_0^T \exp\left(-\frac{E_i}{RT}\right) dT\right]^{1/(1-n_i)}. \quad (4)$$

Table 1
Melter feed composition for high-alumina high-level waste in g kg^{-1} glass.

Chemicals	Mass (g)
$Al(OH)_3$	367.50
H_3BO_3	269.83
CaO	60.80
$Fe(OH)_3$	73.83
Li_2CO_3	88.30
$Mg(OH)_2$	1.70
NaOH	99.53
SiO_2	305.03
$Zn(NO_3)_2{\cdot}4H_2O$	2.67
$Zr(OH)_4{\cdot}0.654H_2O$	5.50
Na_2SO_4	3.57
$Bi(OH)_3$	12.80
Na_2CrO_4	11.13
KNO_3	3.03
$NiCO_3$	6.33
$Pb(NO_3)_2$	6.17
$Fe(H_2PO_2)_3$	12.43
NaF	14.73
$NaNO_2$	3.40
$Na_2C_2O_4{\cdot}3H_2O$	1.30
Total	1349.6

Using Murray and White's approximation [21] for the exponential integral, Eq. (4) becomes

$$\alpha_i = 1 - \left[1 + \frac{(n_i-1)A_i RT^2}{E_i\beta}\left(1-\frac{2RT}{E_i}\right)\exp\left(-\frac{E_i}{RT}\right)\right]^{1/(1-n_i)}. \quad (5)$$

Note that, for $n_i = 1$, A_i can be represented by [20]

$$A_i = \frac{1}{n_i}\frac{E_i\beta}{RT_{\mathrm{im}}^2}\exp\left(\frac{E_i}{RT_{\mathrm{im}}}\right). \quad (6)$$

With E_i from Eqs. (3) and (6), and an initial estimate of n_i ($n_i \neq 1$), Eq. (5) can be utilized to determine initial guesses of α_i as a function of T and β.

With ongoing reactions, the DSC essentially measures the total heat flow to the sample from two contributions concurrently: the heat flow associated with the heat capacity of the sample and the heat flow associated with heat of reactions. The simultaneous DSC–TGA measures the total specific heat flow, Q, which, when divided by the rate of heating, attains the heat capacity unit, i.e., heat per unit mass and temperature. Thus, it becomes an "apparent" heat capacity, $c_p^{\mathrm{app}} = Q/\beta$. Its two contributions are the heat capacity of the sample, c_p, and the heat generated/consumed by the reactions:

$$c_p^{\mathrm{app}} = c_p + \Delta H \partial_T \alpha \quad (7)$$

where ΔH is the overall specific reaction enthalpy [18]. Note that, although DSC (or simultaneous DSC–TGA) is not the best technique to measure heat capacities accurately, it can provide an estimate for heat capacity under appropriate experimental conditions (e.g., $\beta \geq 10\,\mathrm{K\,min^{-1}}$) [22,23]. This allowed us to use the total heat flows from the simultaneous DSC–TGA in order to obtain, by Eqs. (2)–(7), the kinetic parameters for individual peaks (i.e., E_i, A_i, n_i, and w_i), as well as ΔH and estimated c_p. To this end, we used the run/rerun technique and the least squares methods.

3. Experimental

Table 1 shows the melter feed composition used in this study. As described elsewhere [3,24], this feed was formulated to vitrify a high-alumina high-level waste to produce glass of the following composition (with mass fractions in parentheses): SiO_2 (0.305), Al_2O_3 (0.240), B_2O_3 (0.152), Na_2O (0.096), CaO (0.061), Fe_2O_3 (0.059), Li_2O (0.036), Bi_2O_3 (0.011), P_2O_5 (0.011), F (0.007), Cr_2O_3

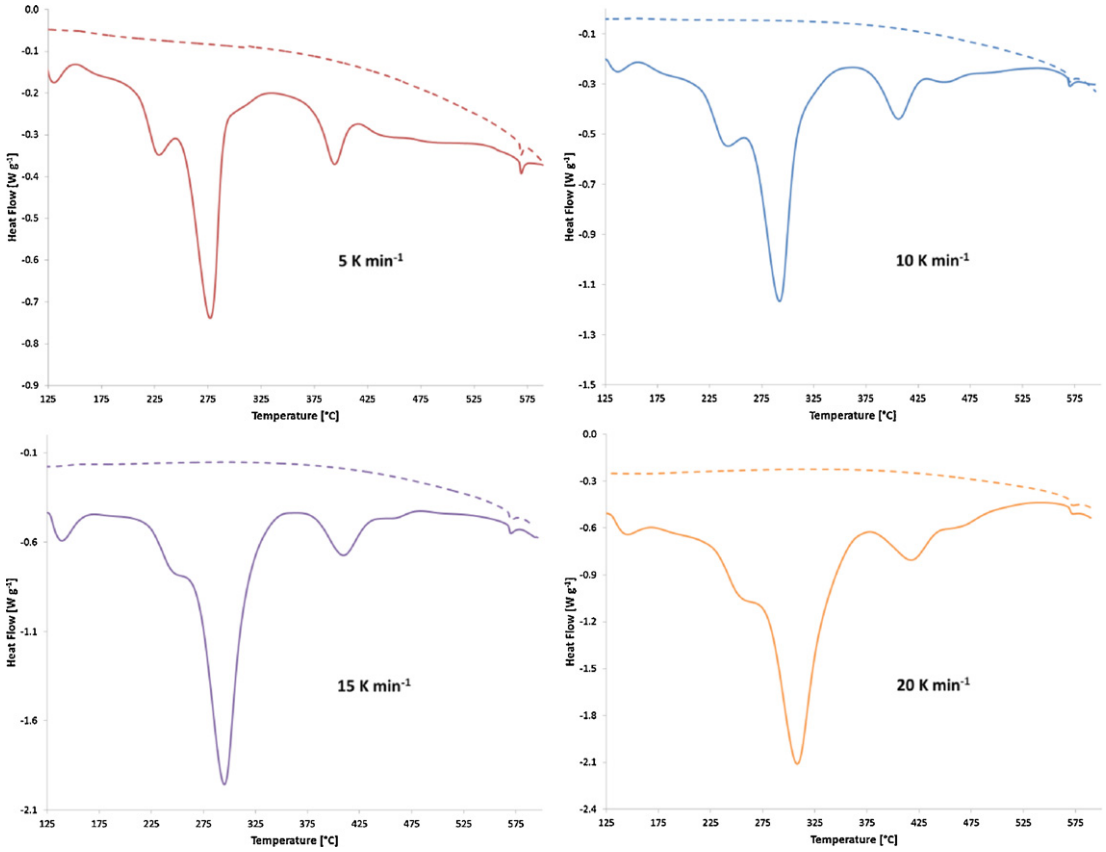

Fig. 1. DSC specific heat flow versus temperature, both first run (solid line) and rerun (dashed line) for heating rates of 5, 10, 15, and 20 K min^{-1}.

(0.005), PbO (0.004), NiO (0.004), ZrO_2 (0.004), SO_3 (0.002), K_2O (0.001), MgO (0.001), and ZnO (0.001). This glass was designed for the Hanford Tank Waste Treatment And Immobilization Plant, currently under construction at the Hanford site in Washington State, USA [25].

The simulated melter feed was prepared as described by Schweiger et al. [24]. The slurry was dried, crushed to a powder, and then placed into an oven at 105 °C overnight. For most experiments with simultaneous DSC–TGA (Model SDT-Q600, TA Instruments, New Castle, DE, USA), a feed sample of 30–50 mg was typically placed in an aluminum crucible and heated from ambient temperature (~25 °C) to 600 °C in the first run. After cooling at about 10 K min^{-1} to 50 °C, the same feed sample was heated again to 600 °C in the rerun step. This run/rerun procedure was repeated for four different heating rates—5, 10, 15, and 20 K min^{-1}. Air was used as a purge gas with a flow rate of 25 ml min^{-1} for all runs. Before any run, the heat flow in the simultaneous DSC–TGA equipment was calibrated, following an equipment guideline, via multiple runs using calibration standards (sapphire disc, Zn metal, Al metal, etc.). As a c_p reference (see below for a method to obtain a specific heat capacity), the run with a ~60 mg sapphire disc (product no. 915079.901, TA instruments) was performed at 10 K min^{-1}. No significant time lag in the run was observed in spite of both a relatively large amount of sample (up to 50 mg) and an alumina crucible. As supporting evidence, the correlation between $\ln(\beta/T_{im}^2)$ and $1/T_{im}$ (i.e., Eq. (3) and/or Fig. 4) was essentially linear, with only one obvious outlier (excluded in the subsequent analysis).

Because the value of heat flow hardly changed between 100 °C and 125 °C, 125 °C was taken as a minimum temperature for analysis to avoid vaporization heat of physically bonded water. The maximum temperature for the simultaneous DSC–TGA experiments was set to 600 °C, above which the limitation of DSC associated with radiation heat losses is well known. In addition, this avoided a possible effect from melt volatilization, which is insignificant in the cold-cap, but affects the heat flow at higher temperatures in the relatively tiny samples used for thermal analysis.

To estimate the heat capacity of the feed as a function of temperature, additional run/rerun combinations were performed at 10 K min^{-1} to final temperatures of 300, 400, and 500 °C; after the first heating to corresponding temperatures and cooling, the feed was heated again up to 200–300 °C in the rerun step. The specific heat capacity of partially reacted feeds was estimated using the relationship $c_p = c_{p,\mathrm{sapp}}(Q/Q_{\mathrm{sapp}})$, where the subscript "sapp" denotes sapphire. Note that $c_{p,\mathrm{sapp}}/Q_{\mathrm{sapp}}$ accounts for a calibration factor equal to $1/\beta$ for perfect calibration, and $c_{p,\mathrm{sapp}}$ is a known heat capacity of sapphire [26]. The heat capacities of the partially reacted feeds at the final temperature, T_f, were estimated from the heat flows of the reruns at T_0 = 100 °C and adjusted to the final temperature by using $c_p(T_f) = c_p(T_0) + [c_{p,q}(T_f) - c_{p,q}(T_0)]$, where $c_{p,q}$ denotes the heat capacity of quartz [26], the major feed component.

4. Results

Fig. 1 shows specific-heat-flow curves for the feed heated at 5, 10, 15, and 20 K min^{-1}. Assuming that all reactions nearly finish during the first run, the heat flow from the rerun presumably corresponds to a heat flow associated with the heat capacity of the feed at the conversion degree reached by a given rate of heating at the final heat-treatment temperature, provided that the continuing chemical reactions have a negligible effect. In addition, the rerun would include the experimental artifacts in the DSC runs, which can thus be eliminated from the first run. Vaporization of molten salts might contribute to the gradual increase in the rerun but cannot account for its full extent; a similar gradual increase in heat flow at

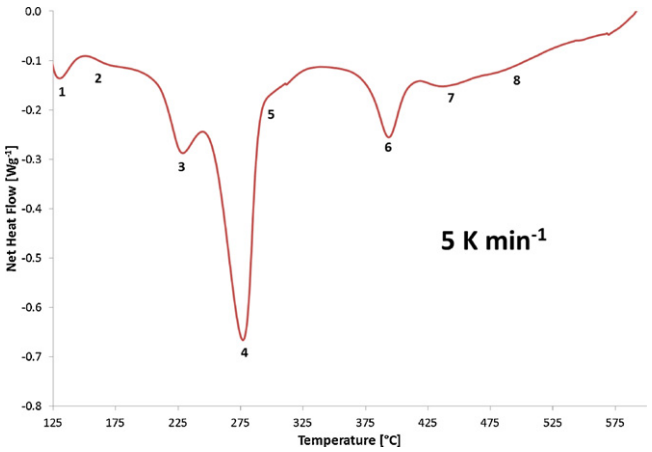

Fig. 2. Net DSC heat flow curve for 5 K min^{-1} with numbers representing identified peaks.

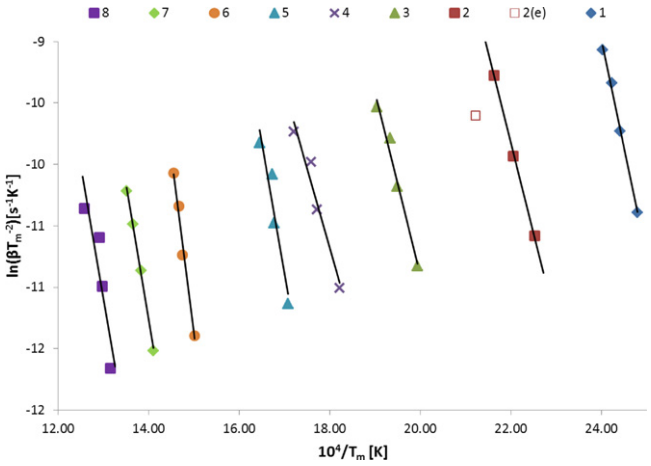

Fig. 4. Kissinger plot (linear least squares fit) for activation energies of individual reactions from DSC experiments; the reactions are marked as in Fig. 2. One outlier, indicated as "2(e)", was excluded for peak 2 as mentioned in Section 3.

the higher temperature range was also observed with non-reacting materials such as sapphire. Finally, the rerun compensates for the effect of the α- to β-quartz transition at ~575 °C.

Fig. 2 illustrates a net heat flow curve for 5 K min^{-1} obtained by subtracting the heat flow of the rerun from that of the first run; the numbers mark the identifiable peaks. Note that the "shoulders" on the curve are signatures of "hidden" reaction peaks. The total area between the net heat flow curve and the temperature axis is $\beta\Delta H$. Thus, using the formula $\Delta H = \beta^{-1}\int_{T_0}^{T_f} Q\,dT$, we obtained the following values for ΔH: 890 J g^{-1} for 5 K min^{-1}, 902 J g^{-1} for 10 K min^{-1}, 762 J g^{-1} for 15 K min^{-1}, and 734 J g^{-1} for 20 K min^{-1}. The decreasing tendency of these values indicates that the reactions were not fully complete at high heating rates.

Fig. 3 shows the overall reaction rate as a function of T and β. A higher heating rate shifted reactions to a higher temperature, as expected. Because $\int(d\alpha/dt)\,dT = \int \beta\,d\alpha$, the area under the rate curve increases with the heating rate, and the total area equals β.

Fig. 4 shows the Kissinger plots for the eight peaks identified in the net specific heat flow data (e.g., Fig. 2). The peak maxima were determined from the net heat flow curves or estimated for shoulders on larger peaks. Using Eq. (3), the activation energies of the reactions were obtained as slopes of the lines fitted to data; the shifts of T_m caused by the peak overlap have little impact on the slope value [3]. Values of E_i are listed in Table 2 along with the coefficients of determination, R^2.

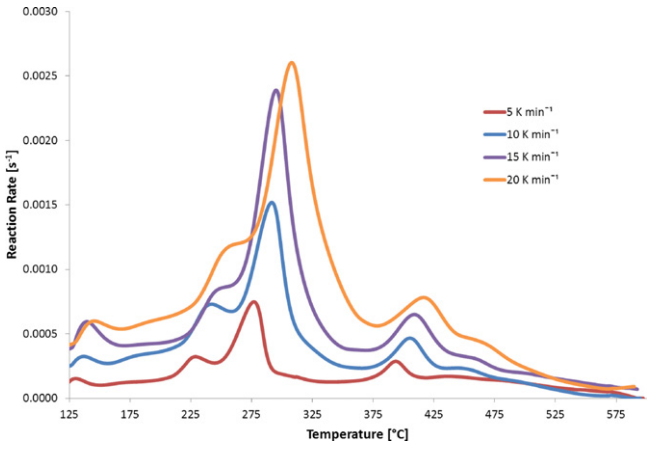

Fig. 3. Overall reaction rates versus temperature for heating rates of 5, 10, 15, and 20 K min^{-1}.

With the activation energies and the overall reaction rates, the least squares analysis was applied for each heating rate to minimize, with an equality constraint $\sum_{i=1}^{N} w_i = 1$, the value of the expression

$$\sum \left[\left(\frac{d\alpha}{dt}\right)_{\text{exp}} - \left(\sum_{i=1}^{N} w_i A_i (1-\alpha_i)^{n_i} \exp\left(-\frac{E_i}{RT}\right) \right)_{\text{cal}} \right]^2$$

where the subscripts "exp" and "cal" denote experimental and calculated values, respectively. Tables 3–5 list the values of the kinetic parameters A_i, n_i, and w_i for individual heating rates with corresponding averages, standard deviations, and relative standard deviations. The small values of standard deviation for $\log(A_i)$ indicate that the pre-exponential factor is essentially independent of the heating rate. The values of the reaction order, $n_i \leq 3$ for all but few peaks, appear to be realistic. The standard deviations of n_i are relatively large, especially for peaks 1, 2, and 7, reflecting the variability of the peak shapes. The values of w_i, shown in Table 5, appear to vary with β and are roughly proportional to corresponding n_i values, as Fig. 5 suggests.

In principle, the values of n_i should be independent of the heating rate because n_i is an intrinsic reaction characteristic. In addition, invariant kinetic parameters are preferable for the cold-cap energy transport model. Table 6 shows values of w_i obtained with averaged values of $\log(A_i)$ and averages of selected (filled symbols in Fig. 5) values of n_i, ignoring extreme values, underlined in Table 4. Fig. 6 compares measured and fitted reaction rates ($d\alpha/dt$). Considering the intricacy of the fitting of 32 parameters and a certain extent of their heating rate dependence, the model appears to yield a reasonable simulation over the 5–20 K min^{-1} range of heating rate.

Table 2
Activation energies with corresponding coefficients of determination, R^2.

Peak	Activation energy [kJ mol^{-1}]	R^2
1	146.84	0.994
2	121.51	0.999
3	123.99	0.978
4	107.39	0.956
5	174.01	0.913
6	243.67	0.988
7	184.57	0.997
8	180.99	0.952

Table 3
Values of $\log(A_i/s^{-1})$ with averages, standard deviations (St. dev), and relative standard deviation (RSD) for peaks 1–8 and four heating rates (β).

β [K min^{-1}]	1	2	3	4	5	6	7	8
5	16.97	12.09	10.61	7.77	13.65	16.85	11.16	9.93
10	16.96	12.07	10.59	7.77	13.65	16.80	11.19	10.05
15	17.00	11.68	10.67	7.86	13.79	16.86	11.18	10.17
20	16.96	12.09	10.59	7.75	13.64	16.84	11.16	9.96
Average	16.97	11.98	10.62	7.79	13.68	16.84	11.17	10.03
St. dev	0.02	0.17	0.03	0.04	0.06	0.02	0.01	0.09
RSD	0.001	0.014	0.003	0.006	0.005	0.001	0.001	0.009

Table 4
Values of the reaction order (n_i) with averages, standard deviations (St. dev), and relative standard deviation (RSD) for peaks 1–8 and four heating rates (β). The underlined values (see Fig. 6) were excluded from further analysis.

β [K min^{-1}]	1	2	3	4	5	6	7	8
5	1.47	2.71	0.65	0.35	4.38	0.78	3.17	2.46
10	1.41	5.18	0.83	0.38	3.01	0.98	2.06	1.36
15	3.11	5.10	0.74	0.38	2.55	1.77	0.62	2.28
20	2.96	2.43	2.28	0.35	2.49	2.15	1.23	1.88
Average	2.24	3.85	1.12	0.37	3.11	1.42	1.77	2.00
St. dev	0.80	1.29	0.67	0.02	0.76	0.56	0.96	0.42
RSD	0.36	0.33	0.60	0.04	0.25	0.39	0.54	0.21

Table 5
Values of w_i with averages, standard deviations (St. dev), and relative standard deviation (RSD) for peaks 1–8 and four heating rates (β).

β [K min^{-1}]	1	2	3	4	5	6	7	8
5	0.043	0.083	0.079	0.252	0.231	0.067	0.164	0.081
10	0.047	0.187	0.098	0.253	0.223	0.076	0.100	0.015
15	0.106	0.129	0.053	0.242	0.250	0.117	0.023	0.079
20	0.079	0.083	0.185	0.128	0.319	0.118	0.050	0.039
Average	0.069	0.121	0.104	0.219	0.256	0.094	0.084	0.054
St. dev	0.025	0.043	0.050	0.053	0.038	0.023	0.054	0.028
RSD	0.370	0.355	0.477	0.240	0.147	0.248	0.641	0.518

Table 6
Optimized w_i values with averaged $\log(A_i/s^{-1})$ values and averages of selected n_i s. Averages, standard deviations (St. dev) and relative standard deviation (RSD) for a fractional conversion heat from individual reactions, $\Delta H_i = w_i \Delta H$, are also provided.

	1	2	3	4	5	6	7	8
$\log(A_i/s^{-1})$	16.97	11.98	10.62	7.79	13.68	16.84	11.17	10.03
n_i	2.24	2.57	0.74	0.37	2.68	1.42	1.30	2.00
w_i								
β = 5 K min^{-1}	0.058	0.074	0.083	0.252	0.190	0.119	0.059	0.164
β = 10 K min^{-1}	0.067	0.111	0.113	0.253	0.242	0.100	0.064	0.049
β = 15 K min^{-1}	0.088	0.099	0.079	0.279	0.228	0.108	0.051	0.068
β = 20 K min^{-1}	0.070	0.111	0.102	0.156	0.360	0.091	0.072	0.039
Average	0.071	0.099	0.094	0.235	0.255	0.104	0.062	0.080
St. dev	0.011	0.015	0.014	0.047	0.063	0.011	0.008	0.050
RSD	0.154	0.154	0.149	0.199	0.248	0.101	0.124	0.620
ΔH_i [J g^{-1}]	57.65	80.57	77.69	195.04	206.37	86.16	50.47	67.72
St. dev [J g^{-1}]	6.56	12.66	15.26	46.70	38.29	14.28	7.04	46.03
RSD	0.11	0.16	0.20	0.24	0.19	0.17	0.14	0.68

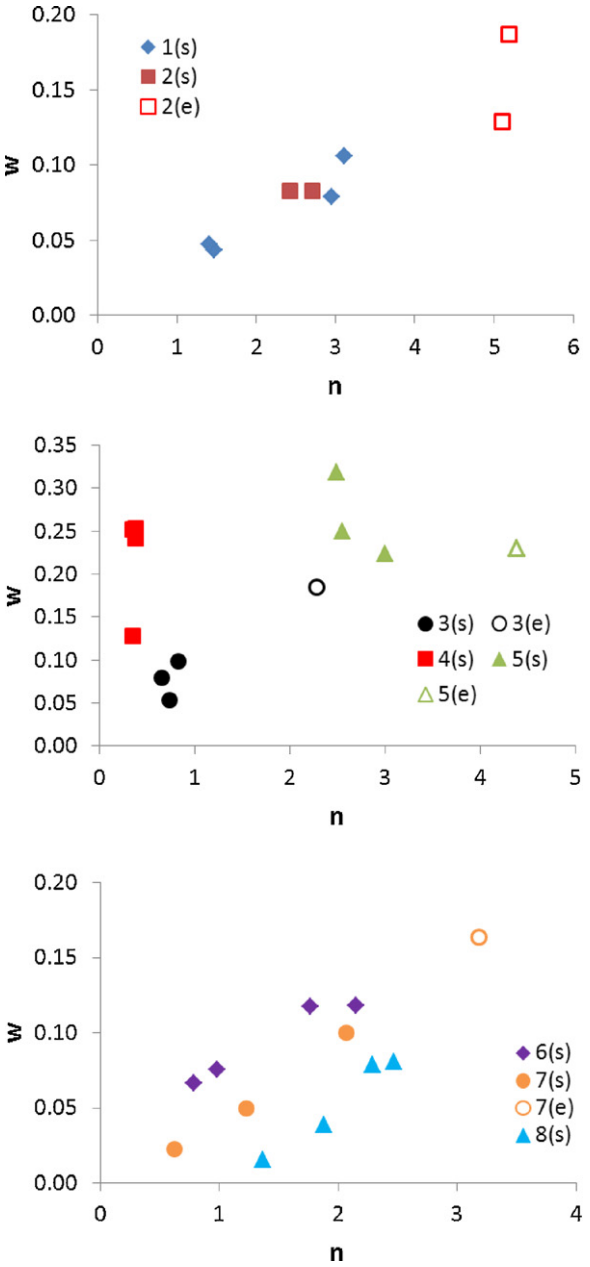

Fig. 5. Distribution of w_i versus n_i, obtained from the least squares analysis at heating rates 5, 10, 15, and 20 K min^{-1} for reactions shown in the legend. Filled and unfilled symbols denote data selected and excluded for average n_i s, indicated as "(s)" and "(e)" respectively.

5. Discussion

5.1. Effect of β on w_i

Slow reactions occurring at lower temperatures may persist to an appreciable extent at low heating rates but may not be noticeable at higher heating rates. Thus, w_i of these reactions can be a decreasing function of β. With more data, a possible way to incorporate interactions between reactions would be to use $w_i(\beta)$ approximation functions while keeping the values of A_i and n_i invariant.

Variation of w_i with β would be inconsistent with the superposition relation, Eq. (2). However, after averaged values of A_i and n_i were employed–compare RSDs shown in Tables 5 and 6–no systematic trends were observed. Thus, the fluctuations of w_i, and hence of individual conversion heats, $\Delta H_i = w_i \Delta H$, may result from random errors associated with experimental uncertainties caused by the small size of the samples (~30 mg). Hence, the superposition relation, Eq. (2), appears to be an acceptable assumption. The largest deviation of w_i occurred for peak 8 in the sample heated at 5 K min^{-1}.

5.2. Comparison between fractional heat- and mass-based kinetic analyses

A similar kinetic analysis was performed previously on the same feed using TGA [3]. Fig. 7 compares DSC and TGA curves for 10 K min^{-1}. In both curves, the positions of most peaks match reasonably: peak 3 at 240 °C, peak 4 at 292 °C, peak 5 (a shoulder) at 323 °C, peak 6 at 405 °C, and peak 7 (a shoulder) at 450 °C. However, discrepancies exist. Such discrepancies can be attributed to three factors. First, not all batch reactions evolve gases. For example, peak 1 was detected by DSC, not by TGA—see Fig. 7. Second, enthalpies of gas-evolving reactions are not necessarily in the proportions of the amounts of gases evolved. For example, reactions between 375 °C and 475 °C (peaks 6 and 7) exhibit a higher extent of conversion with respect to gas evolution than to the reaction enthalpy. Third, differences between the kinetic coefficients (E_i, A_i, and n_i) obtained for TGA and DSC data can be attributed to experimental errors. As is well known, an error in the determination of E_i is compensated by the value of A_i [3]. For example, with the standard error of 20 kJ mol^{-1}, the difference between the highest and lowest E_i estimates can be as high as 40 kJ mol^{-1}. For a peak at ~175 °C, this difference is compensated by the four orders-of-magnitude change in A_i without significantly affecting the data fitting. The standard error of E_i in the TGA experiment was as low as 5 kJ mol^{-1} and as high as 50 kJ mol^{-1} [3]. Accordingly, the differences between E_i obtained for TGA and DSC analyses can be expected to be within this range; E_is from both analyses, in fact, are reasonably correlated within this range, as shown in Fig. 8. In spite of the uncertainty, the parameters are acceptable for the cold-cap modeling because the least squares fitting minimized the overall errors in the kinetic model.

As stated in Section 1, our model approximates the cold-cap reactions as "apparent" *n*th-order reactions. Although the complexity of the cold-cap reactions precludes understanding of their molecular mechanisms, the model is well suited for practical applications in situations, such as that within the cold cap, where the rate of heating varies with temperature within the model validity limits. Also, modeling the mass and energy transport within the cold-cap requires the reaction kinetics equations to be as simple as possible and with minimum parameters.

5.3. Heat capacity of reacting feed

The c_p of the feed estimated via fractional contributions of major components from Table 1 (i.e., $Al(OH)_3$, H_3BO_3, CaO, $Fe(OH)_3$, Li_2CO_3, NaOH, and SiO_2 to cover ~94% of total mass) [27,28] is ~1.3 J g^{-1} K^{-1} at 100 °C. Some of the chemical components of the dry feed were altered by chemical reactions that took place when the batch chemicals were mixed to make slurry that was subsequently dried, but the effect of these reactions on c_p of the feed is small. We also estimated the heat capacity of reacting feed using Eq. (7). At 100 °C, $\Delta H \partial_T \alpha = 0.18$ J g^{-1}·K^{-1} (using ΔH from the integration of the heat flow at 10 K min^{-1} and $\partial_T \alpha$ from the kinetic model, respectively) and $c_p^{app} = 1.43$ J g^{-1} K^{-1} (from the first run at 10 K min^{-1}); thus, by Eq. (7), $c_p = 1.25$ J g^{-1} K^{-1}. However, during

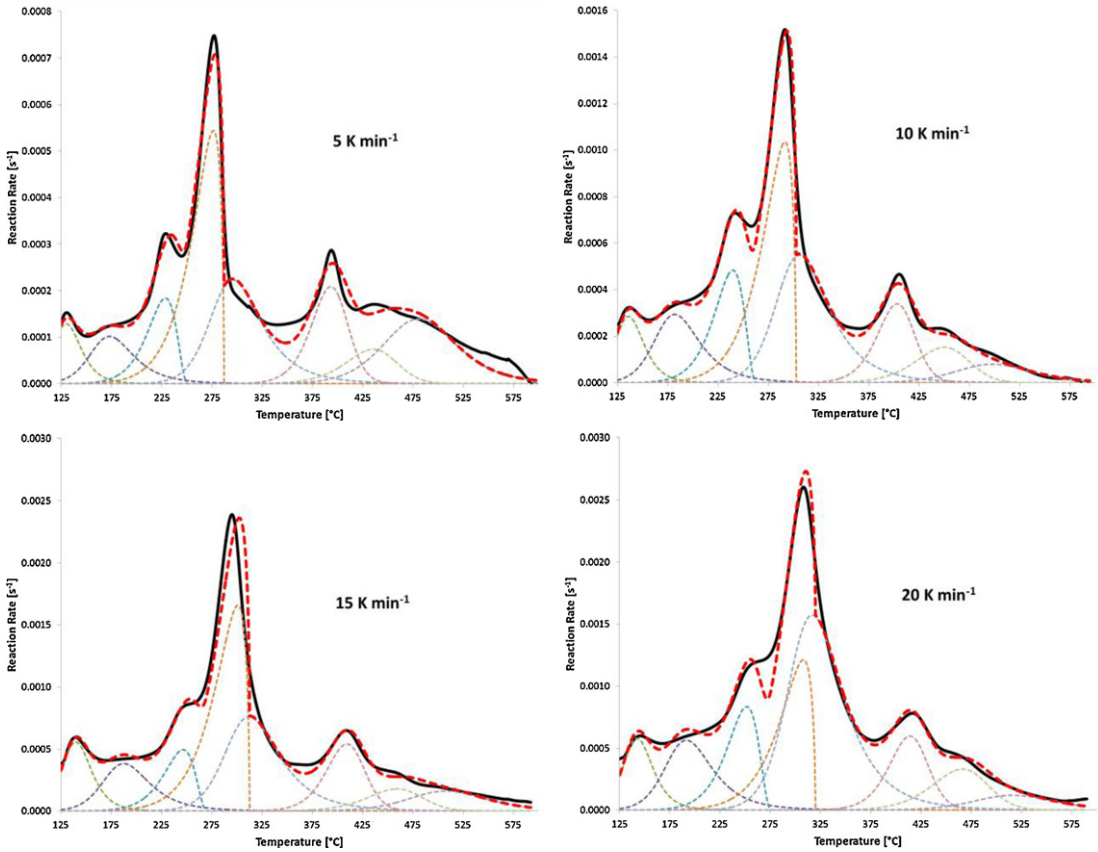

Fig. 6. Measured (solid lines) and fitted (dashed lines) overall reaction rates, along with individual reaction peaks, based on the averaged values of $\log(A_i/s^{-1})$ and averages of selected values of n_i.

the conversion of the dry feed to molten glass, $\Delta H\partial_T\alpha$ and c_p have comparable values of $\sim O(1)\,J\,g^{-1}\,K^{-1}$.

The c_p s from the partially reacted feed at 300, 400, and 500 °C (i.e., measured at 100 °C and adjusted to the final temperatures, as explained in Section 3) are 1.10, 1.11, and 0.95 $J\,g^{-1}\,K^{-1}$, i.e., $1.05 \pm 0.09\,J\,g^{-1}\,K^{-1}$ on average, a value comparable to the c_p of solid borosilicate glasses ($\sim 1\,J\,g^{-1}\,K^{-1}$ [29,30]). The higher c_p at 100 °C may be attributed to the presence of bonded water in several feed components.

The heat flows of the reruns shown in Fig. 1 show rapid changes at temperatures above 425 °C, suggesting an increase in the apparent c_p. This may be an effect combined with the impact of the glass transition. In the feed undergoing heterogeneous reactions, compositional variability ranges from borate glass to glass saturated with silica [24]; thus, the glass transition interval may be stretched over an extended range of temperatures.

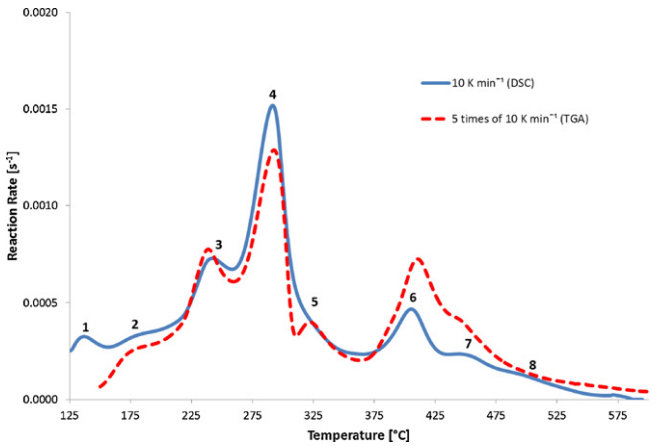

Fig. 7. Comparison between the DSC (solid line) and TGA (dashed line) curves for 10 K min^{-1}. The TGA response [3] was multiplied by 5 because $\sum_{i=1}^{N} w_i^{TGA} = 0.20$ whereas $\sum_{i=1}^{N} w_i^{DSC} = 1$. The numbers represent the DSC peaks as in Fig. 2.

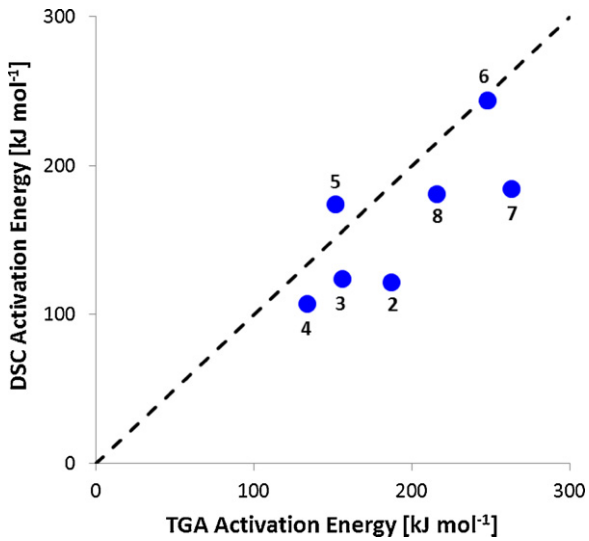

Fig. 8. Activation energies by DSC versus the TGA counterparts obtained from an independent experiment [3]. Numbers indicate peaks seen in Fig. 7; DSC peak 1 has no TGA counterpart. The identity line is dashed.

6. Conclusions

A complete understanding of the cold-cap reactions would require the individual reactions between various granular solids and ionic and glass-forming melts to be identified and their mechanisms to be elucidated. But the complexity of the cold-cap reactions renders such a kinetic model intractable. We instead approximated the multiple overlapping cold-cap reactions as a superposition of *n*th-order kinetic processes. This "phenomenological" or "apparent" model relates the overall conversion rate to temperature and heating rate in a way that satisfactorily defines a constitutive relationship for the energy transport within the cold-cap in a waste glass melter. We used simultaneous DSC–TGA to measure the degree of conversion as a fractional reaction heat and employed the run/rerun technique to minimize the effects of the heat associated with the heat capacity of the feed and experimental artifacts. In addition, the run/rerun to different maximum temperatures provided a way to estimate the c_p of the reacting feed.

Acknowledgements

The authors gratefully acknowledge the financial support of the U.S. Department of Energy Federal Project Office Engineering Division for the Hanford Tank Waste Treatment and Immobilization Plant. Pavel Hrma was supported also by the World Class University program through the National Research Foundation of Korea funded by the Ministry of Education, Science and Technology (R31-30005). Richard Pokorný acknowledges financial support from specific university research (MSMT No 21/2012). The authors greatly appreciate Albert Kruger for his assistance and guidance, and Dong-Sang Kim and Ekkehard Post for insightful discussion and suggestions. Pacific Northwest National Laboratory is operated by Battelle Memorial Institute for the U.S. Department of Energy under contract DE-AC05-76RL01830.

References

[1] R. Pokorný, P. Hrma, Mathematical modeling of cold cap, J. Nucl. Mater. 429 (2012) 245–256.
[2] P. Hrma, A.A. Kruger, R. Pokorný, Nuclear waste vitrification efficiency: cold cap reactions, J. Non-Cryst. Solids (2012), http://dx.doi.org/10.1016/j.jnoncrysol.2012.01.051.
[3] R. Pokorný, D.A. Pierce, P. Hrma, Melting of glass batch: model for multiple overlapping gas-evolving reactions, Thermochim. Acta 541 (2012) 8–14.
[4] F.W. Wilburn, C.V. Thomasson, The application of differential thermal analysis and thermogravimetric analysis to the study of reactions between glass-making materials. Part 1. The sodium carbonate–silica system, J. Soc. Glass Technol. 42 (1958) 158T–175T.
[5] C.V. Thomasson, F.W. Wilburn, The application of differential thermal analysis and thermogravimetric analysis to the study of reactions between glass-making materials. Part 2. The calcium carbonate–silica system with minor batch additions, Phys. Chem. Glasses 1 (1960) 52–69.
[6] F.W. Wilburn, C.V. Thomason, The application of differential thermal analysis and thermogravimetric analysis to the study of reactions between glass-making materials. Part 3. The sodium carbonate–silica system, Phys. Chem. Glasses 2 (1961) 126–131.
[7] F.W. Wilburn, C.V. Thomason, The application of differential thermal analysis and differential thermogravimetric analysis to the study of reactions between glass-making materials. Part 4. The sodium carbonate–silica–alumina system, Phys. Chem. Glasses 4 (1963) 91–98.
[8] F.W. Wilburn, S.A. Metcalf, R.S. Warburton, Differential thermal analysis, differential thermogravimetric analysis, and high temperature microscopy of reactions between major components of sheet glass batch, Glass Technol. 6 (1965) 107–114.
[9] E. Bader, Thermoanalytical investigation of melting and fining of Thüringen laboratory glassware, Silikattechnik 29 (1978) 84–87.
[10] J. Mukerji, A.K. Nandi, K.D. Sharma, Reaction in container glass batch, Ceram. Bull. 22 (1979) 790–793.
[11] O. Abe, T. Utsunomiya, Y. Hoshino, The reaction of sodium nitrate with silica, Bull. Chem. Soc. Jpn. 56 (1983) 428–433.
[12] T.D. Taylor, K.C. Rowan, Melting reactions of soda-lime-silicate glasses containing sodium sulfate, J. Am. Ceram. Soc. 66 (1983) C227–C228.
[13] M. Lindig, E. Gehrmann, G.H. Frischat, Melting behavior in the system SiO_2–K_2CO_3–$CaMg(CO_3)_2$ and SiO_2–K_2CO_3–PbO, Glastech. Ber. 58 (1985) 27–32.
[14] C.A. Sheckler, D.R. Dinger, Effect of particle size distribution on the melting of soda-lime-silica glass, J. Am. Ceram. Soc. 73 (1990) 24–30.
[15] K.S. Hong, R.E. Speyer, Thermal analysis of reactions in soda-lime-silicate glass batches containing melting accelerants: I. One- and two-component systems, J. Am. Ceram. Soc. 76 (1993) 598–604.
[16] K.S. Hong, S.W. Lee, R.E. Speyer, Thermal analysis of reactions in soda-lime-silicate glass batches containing melting accelerants: II. Multicomponent systems, J. Am. Ceram. Soc. 76 (1993) 605–608.
[17] J. Farjas, P. Roura, Isoconversional analysis of solid state transformations: a critical review. II Complex transformations, J. Therm. Anal. Calorim. 105 (2011) 767–773.
[18] M. Reading, A. Luget, R. Wilson, Modulated differential scanning calorimetry, Thermochim. Acta 238 (1994) 295–307.
[19] S. Primig, H. Leitner, Separation of overlapping retained austenite decomposition and cementite precipitation reactions during tempering of martensitic steel by means of thermal analysis, Thermochim. Acta 526 (2011) 111–117.
[20] H.E. Kissinger, Reaction kinetics in differential thermal analysis, Anal. Chem. 29 (1957) 1702–1706.
[21] P. Murray, J. White, Kinetics of the thermal dehydration of clays. IV. Interpretation of the differential thermal analysis of the clay minerals, Trans. Brit. Ceram. Soc. 54 (1955) 204–237.
[22] M.J. O'Neill, Measurement of specific heat functions by differential scanning calorimetry, Anal. Chem. 38 (1966) 1331–1336.
[23] ASTM, E1269-11, Standard Test Method for Determining Specific Heat Capacity by Differential Scanning Calorimetry, ASTM International, West Conshohocken, PA, 2003.
[24] M.J. Schweiger, P. Hrma, C.J. Humrickhouse, J. Marcial, B.J. Riley, N.E. TeGrotenhuis, Cluster formation of silica particles in glass batches during melting, J. Non-Cryst. Solids 356 (2010) 1359–1367.
[25] P.R. Hrma, M.J. Schweiger, B.M. Arrigoni, C.J. Humrickhouse, J. Marcial, A. Moody, C. Rodriguez, R.M. Tate, B. Tincher, Effect of Melter-Feed-Makeup on Vitrification Process, PNNL-18374, Pacific Northwest National Laboratory, Richland, Washington, 2009.
[26] D.A. Ditmars, S. Ishihara, S.S. Chang, G. Bernstein, E.D. West, Enthalpy and heat-capacity standard reference material: synthetic sapphire (α-Al_2O_3) from 10 to 2250 K, J. Res. Nat. Bur. Stan. 87 (1982) 159–163.
[27] M.W. Chase Jr., NIST-JANAF Themochemical Tables, 4th ed., CT J. Phys. Chem. Ref. Data, Monograph 9, American Institute of Physics, Melville, New York, 1998, pp. 1–1951.
[28] J.L. Haas Jr., G.R. Robinson Jr., B.S. Hemingway, thermodynamic tabulations for selected phases in the system CaO–Al_2O_3–SiO_2–H_2O, Open-File Report 80-908, U.S. Geological Survey, Reston, Virginia, 1980.
[29] H. Scholze, Glasses: Nature, Structure, and Properties, Springer-Verlag, Berlin, 1991, pp. 355–360.
[30] N.P. Bansal, R.H. Doremus, Handbook of Glass Properties, Academic Press, London, 1986, pp. 179–206.